Integrated numerical and laboratory rock physics applied to seismic characterization of reservoir rocks

Beatriz Quintal, Marcel Frehner, Claudio Madonna, Nicola Tisato, Maria Kuteynikova, and Erik H. Saenger, ETH Zurich

A good understanding of the effect of rock and pore-fluid properties on seismic waves is necessary for the characterization of a subsurface hydrocarbon reservoir from a seismic data set. Information about the rock and fluids in the reservoir can be obtained, for example, through well logging and laboratory tests with samples cored from the wellbore. Together with seismic data, this information can be extrapolated for the entire dimension of the reservoir to provide valuable quantitative estimates for production. Additionally, this information can be extrapolated in time for monitoring the spatial redistribution of fluids during production. Making such space and time extrapolations more accurate using seismic data is the main goal of rock physics. For that, identifying and understanding the physical processes taking place in a reservoir rock at different scales is an important step and the subject of our article.

We show that the integration of laboratory studies with numerical modeling is a powerful tool to achieve an unbiased understanding of the physical processes at different scales. In laboratory experiments, it is very difficult, and in some cases even impossible, to control all the physical processes. However, in numerical simulations all physical parameters can be controlled exactly, and it is even possible to separately study different physical processes which otherwise coexist in nature or in the laboratory. The physical insight resulting from such numerical studies helps understand and better interpret results from laboratory experiments. This knowledge-feedback between laboratory and numerical rock physics is demonstrated in this article on examples of two current challenges in rock physics: understanding the influence of the rock microstructure on effective elastic properties, and identifying the dominant physical mechanism responsible for intrinsic attenuation in rocks at seismic frequencies

Both challenges are subject to ongoing research conducted in The Rock Physics Network at ETH Zurich and the studies presented in this article are a snapshot of work in progress. Indeed, the research progress on the two challenges is quite different. While the first is well advanced and understood, the second still remains a considerable challenge. Nevertheless, we demonstrate how such challenges can be tackled by combining laboratory and numerical rock physics techniques.

Effect of the rock microstructure on effective elastic properties

X-ray microcomputed tomography (micro-CT) allows 3D imaging of the microstructure of a rock (insets in Figure 1; Dvorkin et al., 2008; Knackstedt et al., 2009; Saenger et al., 2011). Numerical model-

ing using such digital rock models, combined with laboratory measurements, can be used to predict properties of a reservoir rock, such as flow and elastic properties. Simulating fluid flow through digital rock models using, for example, the Lattice-Boltzmann method (e.g., Narváez et al., 2010) can now be done successfully, with the predicted permeability being in reasonable agreement with laboratory measurements (Dvorkin et al., 2008). In this case, the resolution of the micro-CT technique may be sufficient because fluid pathways predominantly follow larger pores. On the other hand, mechanical properties, such as the effective elastic moduli, strongly depend on the microstructural details of the rock (e.g., Kuster and Toksöz, 1974; O'Connell and Budiansky, 1974; Smith et al., 2009; Ruiz and Cheng, 2010), which might not be resolved by the micro-CT technique. The inability to fully characterize the microstructural details of a rock can lead to disagreements between numerical estimates of mechanical properties and laboratory data. In the following, we describe a method to successfully resolve this problem. The presented case study consists of laboratory measurements and numerical simulations to determine the P-wave velocity at 3 MHz in a sample of Berea sandstone. The corresponding wavelength is much larger than the pore size. Laboratory experiments are coupled with numerical
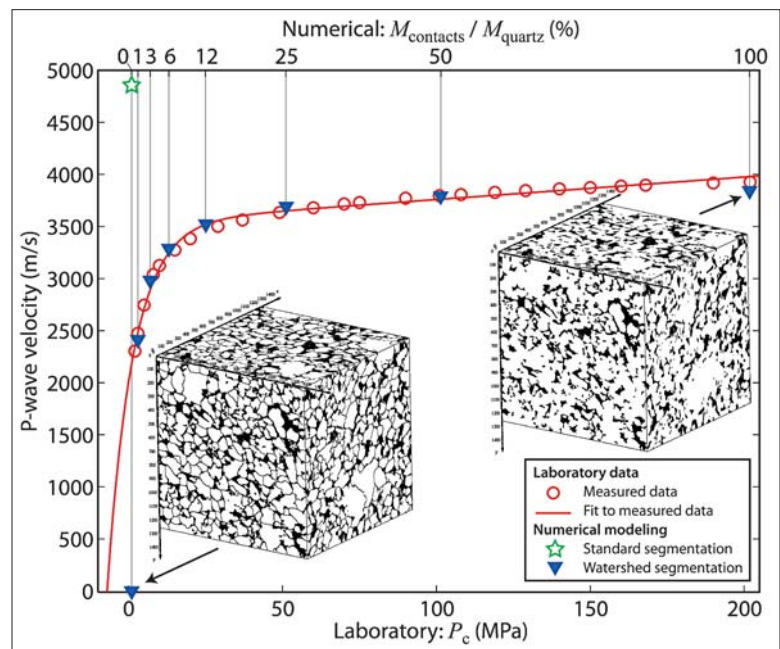

Figure 1. *Laboratory and numerical results for the P-wave velocity at 3 MHz as a function of confining pressure, P_c, in a Berea sandstone sample. P-wave velocity is obtained by numerical wave-propagation modeling through a digital rock model generated by standard segmentation of micro-CT data (star) and watershed segmentation (triangles). The grain contacts identified by the watershed segmentation have a P-wave modulus, $M_{contacts}$, ranging from 0% to 100% of the P-wave modulus of quartz, M_{quartz} (upper abscissa). The left and right insets shows the 3D digital rock model containing grain contacts with a P-wave modulus equal to zero and M_{quartz}, respectively. The cube volume is 2 cm^3.*

simulations to provide an understanding of the effect of the rock microstructure on the resulting velocity.

Laboratory experiments. P-wave velocity was measured at a frequency of 3 MHz on a dry sample of Berea Sandstone (25.4 mm diameter, 40 mm length) using the pulse-transmission technique at confining pressures up to 200 MPa at room temperature. The experiments were performed in a Paterson gas-medium apparatus, where a copper jacket isolates the sample from the confining argon gas. Because the pore pressure is negligible, the confining pressure is equal to the effective pressure. The resulting curve (open circles and solid line in Figure 1) describes a nonlinear increase of the P-wave velocity, V_p, with confining pressure, P_c, up to 50 MPa, followed by a linear trend for higher confining pressures.

Numerical experiments. X-ray micro-CT imaging was performed on a core plug of 6 mm diameter and 20 mm length of the same Berea sandstone sample used in the laboratory experiments. The system consists of a SkyScan 1172 high-resolution desktop scanner providing a pixel size of 3.14 μm. One complete data set consists of 1400 cross sections. A standard segmentation technique divides the raw data (eight-bit tiff images) into three different phases: quartz, which is the main matrix, ankerite, and the empty pores. Other minerals (less than 3% of the matrix volume) were segmented as quartz. The segmented micro-CT data (right inset in Figure 1) provide a 3D digital model of the scanned rock. Table 1 lists the elastic moduli of the minerals, and the pores are treated as vacuum. To obtain the effective P-wave velocity in the digital rock model, we use the rotated staggered finite-difference method to propagate a plane P-wave with a central frequency of 3 MHz through the 3D digital rock model (Saenger et al., 2011, and references therein). By measuring the time-delay of the peak amplitude between two planes of receivers, we calculate the effective P-wave velocity, V_p. The result of this first modeling approach using standard segmentation is shown in Figure 1 as a star.

Integrated interpretation of laboratory and numerical results. In Figure 1, the result from the first numerical modeling approach (star) disagrees with the laboratory measurements (open circles). On one hand, the P-wave velocity calculated from the digital rock model is higher than all laboratory measurements, an observation already reported in recent studies (e.g., Knackstedt et al., 2009). On the other hand, it is unclear to which confining pressure the calculated P-wave velocity corresponds (it is arbitrarily plotted at zero confining pressure in Figure 1). A more detailed characterization of the rock microstructure reveals the cause of this discrepancy. Mercury intrusion porosimetry (Figure 2), with a resolution down to 1 nm, demonstrates that pores with a size of 10 μm dominate the pore volume, but it also shows that around 25% of the pore volume is below the resolution limit of the micro-CT imaging technique. Scanning electron microscope (SEM) images (Figure 3), with a resolution down to 0.1 μm, reveal that two main features remain unresolved in the micro-CT digital rock model: the grain-contacts and microcracks within grains. These mechanically weaker parts are not taken into account
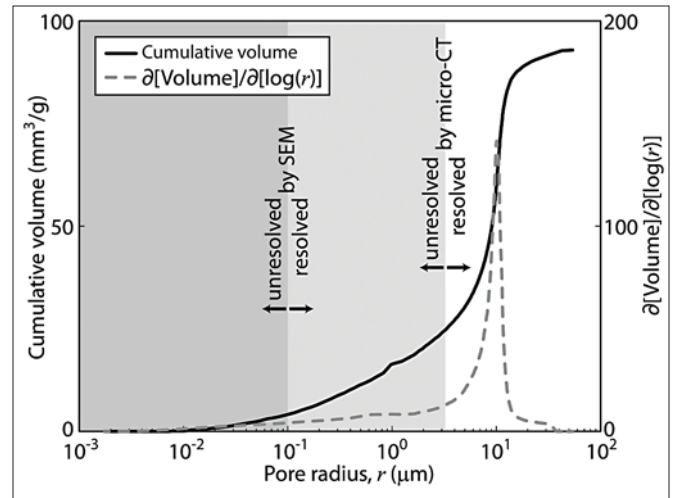

Figure 2. *Mercury porosimetry measurements from a Berea sandstone sample of 10 cm³ and resolution limits of SEM and micro-CT. The cumulative intruded mercury volume is given per gram of solid rock. The dashed curve is the derivative of the cumulative volume versus pore radius curve (solid line).*

during the numerical simulation. However, it is known that both features significantly influence the effective mechanical properties (e.g., O'Connell and Budiansky, 1974; Smith et al., 2009). We therefore assume that the difference between numerical and laboratory results (Figure 1) is mainly due to these unresolved microstructures.

To improve the digital rock model, we apply the so-called watershed segmentation, which is a grain-contact reconstruction method. This method is based on the concept of representing the gray-level intensity of the micro-CT data as topography and a subsequent rainfall onto this topography, hence watershed (e.g., Arns et al., 2007). It allows localizing grain contacts that are below the resolution of the micro-CT data. These grain contacts represent an additional phase in the digital rock model compared to the three phases defined by the standard segmentation technique. Figure 4 depicts this fourth phase and it reveals that the grain contacts form a complex interconnected 3D network. In subsequent numerical simulations, an effective P-wave modulus, $M_{contacts}$, with values ranging between 0% and 100% of the P-wave modulus of quartz, M_{quartz} (Table 1), is assigned to the grain contacts because they are assumed to be always weaker than the quartz grains. In this way, a P-wave velocity is obtained as a function of $M_{contacts}/M_{quartz}$ (triangles as a function of upper abscissa in Figure 1). If $M_{contacts}$ is zero (left inset in Figure 1), the grain contact phase represents a vacuum and the resulting P-wave velocity is zero. If $M_{contacts}$ is equal to M_{quartz} (right inset in Figure 1), the grain contact phase is effectively nonexistent. This case is equivalent to using the standard segmentation method, for which no grain contacts are identified.

The resulting numerical curve ($V_{P,num}$ versus $M_{contacts}/M_{quartz}$) shows a similar trend as the laboratory measurements ($V_{P,lab}$ versus P_c), such that a linear data mapping between the two data sets can be assumed. The data pairs are linearly

	Density ρ (kg/m³)	Bulk modulus K (GPa)	Shear modulus G (GPa)	P-wave modulus M* (GPa)
Quartz	2648	37.8	44.3	96.89
Ankerite	2712	73.3	32	115.97
*M = K + 4G/3				

Table 1. *Elastic moduli of crystals at room pressure and temperature.*

mapped according to

$$\left\{ \begin{array}{c} V_{lab} \\ P_c \end{array} \right\} = \left\{ \begin{array}{c} sV_{num} \\ b + aM_{contacts} \end{array} \right\}. \tag{1}$$

Parameters s, b, and a are fitted simultaneously by minimizing the least-squares misfit to the laboratory data. The resulting values are $s = 0.7919$, $b = 0.9743$ MPa, and $a = 2.0086$. The resulting pressure-dependent velocity ($V_{P,num}$ versus P_c) is shown in Figure 1 as triangles as a function of the lower abscissa in Figure 1. This result demonstrates that the P-wave modulus of the grain contacts depends on the confining pressure (i.e., becoming stiffer with increasing pressure) and that a simple linear relation best fits the laboratory measurements up to the investigated confining pressure of 200 MPa. The numerical method systematically overestimates the P-wave velocity by a factor of s compared to the laboratory measurements because of the unresolved microcracks and other microstructures, which cannot be detected with the grain contact reconstruction technique. However, the presented calibration with laboratory data enables the numerical computations to yield not only an accurate prediction of the P-wave velocity with pressure, but also an estimation of the effect of grain contacts on the P-wave velocity. The evaluated parameters in Equation 1 are valid only for the investigated Berea sandstone and probably for similar sandstones.

Physical mechanism for attenuation at seismic frequencies

Attenuation of seismic waves in partially saturated porous rocks is of great interest because it has recently been observed that oil and gas reservoirs frequently exhibit high P-wave attenuation, especially at low seismic frequencies (e.g., Chapman et al., 2006, and references therein). Additionally, several studies have reported on the existence of low-frequency anomalies of seismic reflections associated with hydrocarbon reservoirs (e.g., Taner et al., 1979; Castagna et al., 2003; Korneev et al., 2004; Goloshubin et al., 2006). Some authors have explained these reflection anomalies with a high and frequency-dependent attenuation in the reservoir rocks (Korneev et al., 2004; Quintal et al., 2011a). Saenger et al. (2009) suggest that a frequency-dependent attenuation could also explain low-frequencies anomalies observed in passive seismic data (see also Lambert et al., 2011). When the dominant physical mechanisms for attenuation are identified and understood, estimates of attenuation can improve interpretation (and inversion) of seismic data. Because high and frequency-dependent attenuation is generally associated with the presence of pore fluids,
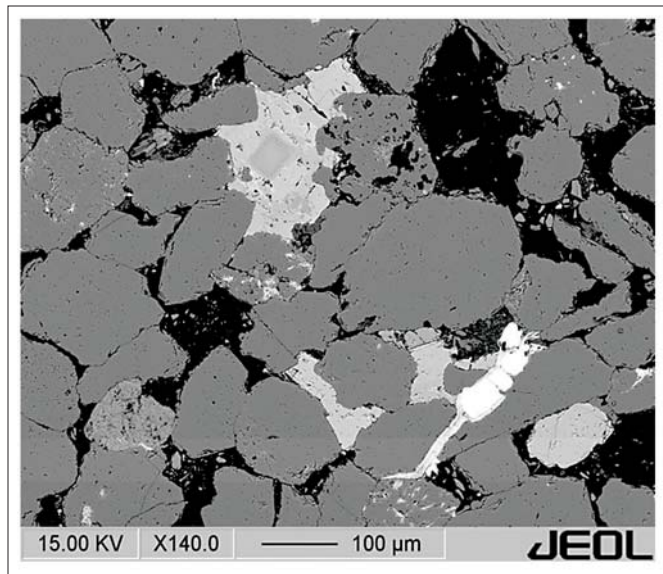

Figure 3. *Scanning electron microscopy (SEM) image of a Berea sandstone slice. Gray levels correspond to different mineral phases; black colors are voids. Grain contacts and microcracks are clearly identified.*

information about the fluid such as fluid type or saturation may be inferred from such advanced seismic studies.

In the following, we explain the self-developed laboratory apparatus used to measure intrinsic bulk attenuation in a partially saturated Berea sandstone sample in the low-frequency range. Additionally, we apply numerical modeling of attenuation caused by the physical mechanism of wave-induced fluid flow to an idealized digital version of the same Berea sandstone sample. The combination of laboratory measurements and numerical simulations is a way to verify or falsify the dominance of this particular physical mechanism for attenuation.

Laboratory experiments. The CAD-model of the self-developed Broad Band Attenuation Vessel (BBAV; Tisato et al., 2011) is shown in Figure 5. The BBAV measures the intrinsic bulk attenuation in a partially saturated rock sample of 25 cm height and 7.6 cm diameter at seismic frequencies by performing a series of subresonance tests at different frequencies ranging from 0.1 to 100 Hz. Due to the quasistatic nature of the experiment, inertial effects are negligible. The BBAV is equipped with two independent pressure systems, the first controlling the confining pressure inside the pressure vessel (up to 25 MPa; black in Figure 5) and the second controlling the sample saturation (blue in Figure 5). Any fluid, for example water or oil, can be pumped as pore fluid into the closed BBAV. A vacuum burette allows controlling the amount of pore fluid saturating the sample. The applied strain is kept lower than 2×10^{-6} because these values can be expected for natural seismic waves and attenuation is assumed to be linear under such low strains. Calibration of the BBAV has been successfully performed with two end-member reference samples: (1) aluminum, which is almost perfectly elastic and exhibits attenuation approaching zero and (2) plexiglas, which exhibits high attenuation in the frequency range of interest. These results give us confidence that the measurements are valid (Ti-

Figure 4. *Micro-CT image of the Berea sandstone sample after watershed segmentation. The grain contacts identified by the watershed segmentation are shown. The cube volume is 2 cm³.*

with numerical modeling. Here, we numerically model attenuation caused only by wave-induced fluid flow due to patchy saturation at the mesoscopic scale because this mechanism is generally assumed to dominate attenuation at our frequency range of interest (White, 1975; Pride et al., 2004). In a patchy saturated medium, a seismic wave causes pore-pressure differences between the continuous background rock fully saturated with one fluid and the mesoscopic-scale patches fully saturated with another fluid. These pore-pressure differences are due to the different compressibilities of the two fluids. Viscous pore fluid flows along the pressure gradients, causing attenuation of the seismic wave (Pride et al., 2004). The mesoscopic scale is much larger than the pore size but much smaller than the wavelength and the properties of the solid frame are the same everywhere. A partially saturated porous rock is approximated by such a patchy saturated medium. In the numerical model, both regions are mathematically described by poroelasticity, with different sets of parameters describing the properties of the pore fluids.

sato et al., 2011).

We measured the bulk attenuation in a sample of Berea sandstone with permeability around 600 mD, porosity around 20%, and bulk and shear moduli of the dry frame of 7 GPa and 4.2 GPa, respectively. The measurements reported were performed at room pressure and temperature, even though confining pressures up to 25 MPa are achievable by the BBAV. The sample was sealed from the confining medium (oil) with a latex tube applied around the rock plug. For the reported measurements, the Berea sandstone sample was partially saturated with 60% water and 40% air. Figure 6 shows the measured quality factor, *Q*, as a function of frequency as dots and open circles. The inverse of the quality factor is a measure of attenuation. To achieve the 60% partial water saturation, two different saturation methods were used. In one case, the water saturation in the sample was increased from 0% to 60% (open circles in Figure 6). In the second case (dots in Figure 6), the sample was first saturated with 90% water and the water saturation was then reduced to 60%. The two frequency-dependent attenuation curves from these two experiments exhibit a slight shift, particularly at higher frequencies. Because the same sample was used in both experiments, we infer that the difference between the two laboratory data curves for *Q* is caused by different spatial distributions of water and air in the sample.

Numerical experiments. While in laboratory experiments all possible physical attenuation mechanisms occur simultaneously, we are able to study different mechanisms separately

To calculate attenuation due to wave-induced fluid flow, we numerically perform quasistatic creep tests solving Biot's equations for consolidation. A detailed description of the equations and the methodology is given by Quintal et al. (2011b). The 3D numerical poroelastic sample (Figure 7) has the same dimensions as the sample used in the laboratory experiments (25 cm height, 7.6 cm diameter). Three equally spaced spherical heterogeneities in fluid-saturation are aligned at the center of the sample to represent the patchy saturation. The properties of the solid frame (Table 2) are the same everywhere, and the same as the bulk properties of the laboratory sample. We consider this a reasonable approximation because the Berea sandstone sample used in our study has a homogeneous solid frame. For the partial water saturation, two scenarios were chosen: (1) fully air-saturated heterogeneities and fully water-saturated surrounding rock (solid line in Figure 6); and (2) fully water-saturated heterogeneities and fully air-saturated surrounding rock (dashed line in Figure 6). For both cases, the radius of the three spherical heterogeneities is chosen such that a 60% water saturation of the whole sample is achieved. For performing the numerical quasistatic creep tests on the

Solid frame	Berea sandstone	
Permeability (mD)	600	
Porosity	0.20	
Bulk modulus of the dry frame (GPa)	7	
Shear modulus of the dry frame (GPa)	4.2	
Bulk modulus of the solid grains (GPa)	36	
Density of the solid grains (kg/m³)	2650	
Fluid	Water	Air
Bulk modulus of the fluid (GPa)	2.2	10^{-4}
Density of the fluid (kg/m³)	1000	1
Viscosity of the fluid (Pa·s)	0.001	2×10^{-5}

Table 2. *Petrophysical parameters used for numerically modeling attenuation in a partially saturated rock sample.*

Figure 5. *CAD-model of the Broad Band Attenuation Vessel (BBAV) used for laboratory seismic attenuation measurements. Note that the bulk attenuation, and not a local attenuation, is measured with the applied strain sensor.*

Figure 6. *Laboratory and numerical results for the frequency-dependent quality factor (Q) for a Berea sandstone sample saturated with 60% water and 40% air. Two saturation methods were applied in the laboratory: (1) increase of the water saturation in the dry sample from 0% to 60% (open circles); and (2) reduction of an initial 90% water saturation down to 60% (dots). In the numerical model, two saturation scenarios were chosen: (1) fully air-saturated heterogeneities in fully water-saturated surrounding rock (solid line); and (2) fully water-saturated heterogeneities in fully air-saturated surrounding rock (dashed line). The minimum Q-value is outside the shown axes at the transition frequency, f_{tr}. Triangular symbols illustrate the slopes in double-logarithmic axes.*

3D model, we use the COMSOL Multiphysics finite-element software. The resulting frequency-dependent attenuation (Figure 6), which is solely due to wave-induced fluid flow, almost perfectly coincides for the two saturation scenarios. Only at higher frequencies approaching the transition frequency (f_{tr} = 6 kHz) do the two curves slightly diverge. The transition frequency is the frequency at which the minimum value of Q, Q_{min}, occurs and is controlled mainly by permeability, fluid viscosity, and patch size. The theoretically predicted slope of −1 in the double-logarithmic plot and in the low-frequency limit is reproduced by both numerical simulations.

Integrated interpretation of laboratory and numerical results. In the investigated low-frequency range (1–100 Hz), the numerical calculations of the quality factor, Q, disagree with the laboratory measurements (Figure 6). The values of Q are much greater than the values measured in the laboratory experiments. Only above 200 Hz do the values of Q become smaller. We also observe that the slopes of the frequency-dependent attenuation curves are different for the numerical and laboratory data. For the laboratory data, the slope is around −0.25 in double-logarithmic representation. For the numerical calculations, the slope is around −1, which is predicted by the wave-induced fluid-flow theory for a periodic distribution of heterogeneities, and also for a random distribution of heterogeneities in a finite volume (Müller and Rothert, 2006; Quintal et al., 2011b). We don't believe that the low slope observed in the laboratory data is due to inaccuracies in the measurement protocol, due to the extensive testing and calibration of the BBAV (Tisato et al., 2011). In addition, each data-point plotting in Figure 6 is an average of five consecutive measurement series with very low spreading, indicating high reproducibility of the laboratory data (the standard deviation of each measurement is, in average, 10% of the value of Q).

Because, in the numerical simulations, patchy saturation is the only cause of attenuation, the fundamental difference in slope can lead to the conclusion that wave-induced fluid flow is not the sole cause of attenuation in the Berea sandstone
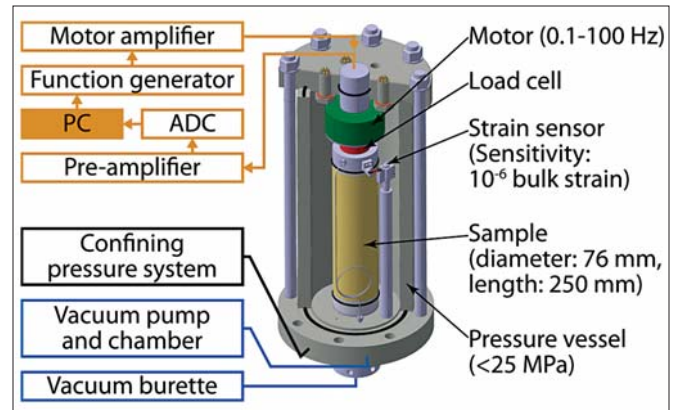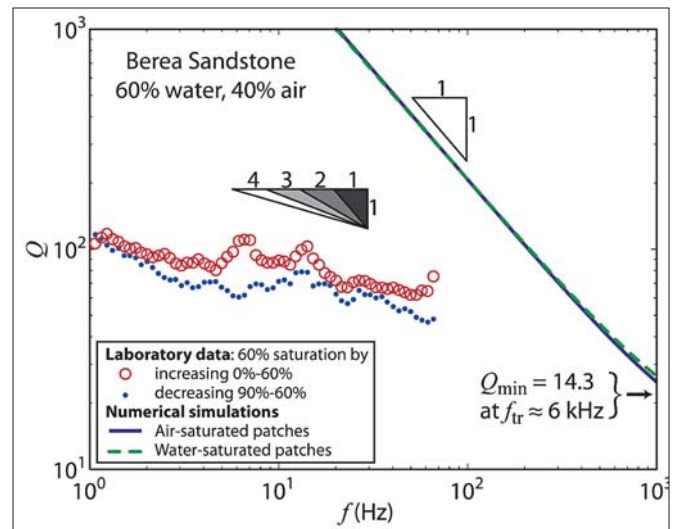
sample. However, it is possible that wave-induced fluid flow is indeed one dominant physical mechanism for attenuation, but the model used for the numerical simulation, consisting of three spherical heterogeneities in fluid saturation and a homogeneous solid frame (Figure 7), may be too much of an oversimplification of the spatial distribution of fluids and of frame properties in the real Berea sandstone sample. For example, micro-CT imaging of partially saturated Berea sandstone (Figure 8) shows that the fluid-distribution geometry is much more complex than the simple approximation used in the numerical model. How more complex (and more realistic)
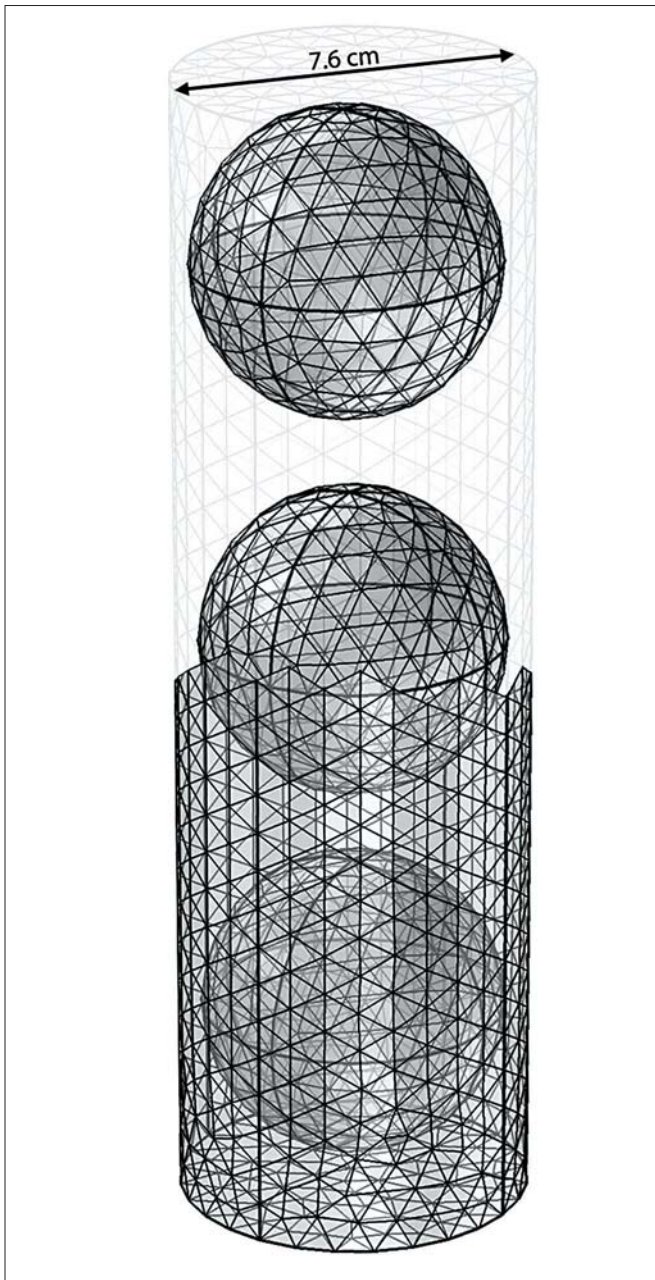
Figure 7. *3D numerical sample with the tetrahedral finite-element mesh used for the numerical simulations. The dimensions are the same as in the laboratory experiments (25 cm height, 7.6 cm diameter). Three equally spaced spherical heterogeneities are defined within the sample to represent the patchy saturation.*

Figure 8. *Micro-CT image of a Berea sandstone slice partially saturated with oil and air. Gray = solid skeleton. White = air-filled pores. Black = oil-filled pores. The diameter of the slice is 6 mm.*

distributions and geometries of the fluid-saturation heterogeneities associated with a heterogeneous solid frame can change the low-frequency attenuation behavior remains to be studied in the future. Other attenuation mechanisms (e.g., squirt flow) must also be investigated individually in future numerical studies.

Conclusions

We presented two ongoing research projects in the field of rock physics, where we integrate laboratory and numerical methods to better understand the relevant physical processes. Based on
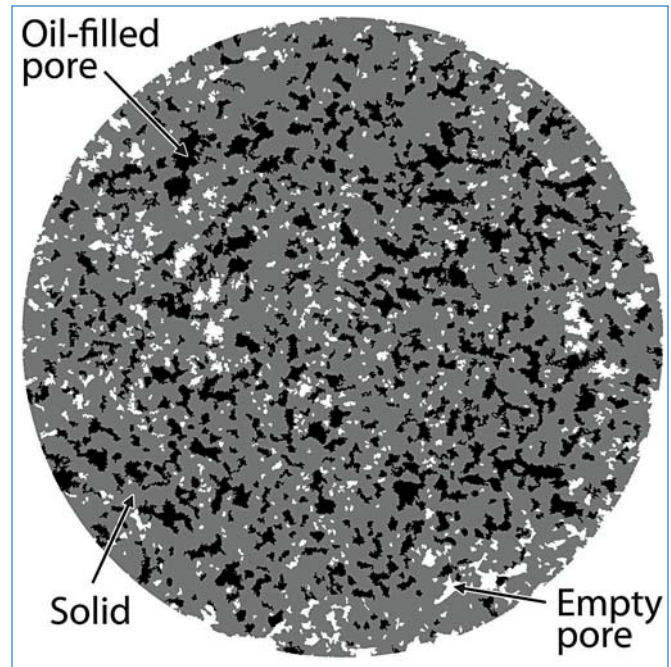
our experience, we would even state that laboratory or numerical studies alone can lead to misconception or misinterpretation of the obtained results. For example, the 3D numerical attenuation modeling presented above could have been overinterpreted if it was not compared to the laboratory data.

The combination of laboratory and numerical methods is essential for successful rock physics research. Modern laboratory equipment, such as the BBAV presented in this article, allows high-precision measurements of various petrophysical parameters and, hence, a precise characterization of the rock. Advanced numerical methods allow studying different physical mechanisms separately from each other to eventually determine the dominant mechanism. Only the combination of the two approaches, laboratory and numerical, provides an unbiased understanding of the underlying physical processes.

Finally, modern imaging methods, such as micro-CT or Synchrotron X-ray tomography, further improve the combination of laboratory and numerical methods. These nondestructive imaging methods allow digitizing the exact same rock sample that is used in laboratory experiments and then performing numerical simulations on its digital rock model. This procedure led to the successful data mapping demonstrated above between laboratory and numerical ultrasonic P-wave velocity data, by which the role of the grain contacts could be studied. The next steps ahead consist of conducting laboratory experiments inside modern tomographic scanners. Scanning and generating a digital rock model under laboratory (and reservoir) conditions for subsequent numerical simulations will allow an even deeper insight into the relevant physical processes taking place in the studied rocks. **TLE**

References

Arns, C. H., M. Madadi, A. P. Sheppard, and M. A. Knackstedt, 2007, Linear elastic properties of granular rocks derived from X-ray-CT images: 77th Annual International Meeting, SEG, Expanded Abstracts, **26**, 1711–1715, doi:10.1190/1.2792823.

Castagna, J. P., S. Sun, and R. W. Siegfried, 2003, Instantaneous spectral analysis: Detection of low-frequency shadows associated with hydrocarbons: The Leading Edge, **22**, no. 2, 120–127, doi:10.1190/1.1559038.

Chapman, M., E. Liu, and X. Li, 2006, The influence of fluid-sensitive dispersion and attenuation on AVO analysis: Geophysical Journal International, **167**, no. 1, 89–105, doi:10.1111/j.1365-246X.2006.02919.x.

Dvorkin, J., M. Armbruster, C. Baldwin, Q. Fiang, N. Derzhi, C. Gomez, B. Nur, and A. Nur, 2008, The future of rock physics: Computational methods vs. lab testing: First Break, **26**, 63–68.

Goloshubin, G., C. Van Schuyver, V. Korneev, D. Silin, and V. Vingalov, 2006, Reservoir imaging using low frequencies of seismic reflections: The Leading Edge, **25**, no. 5, 527–531, doi:10.1190/1.2202652.

Knackstedt, M. A., S. Latham, M. Madadi, A. Sheppard, T. Varslot, and C. Arns, 2009, Digital rock physics: 3D imaging of core material and correlations to acoustic and flow properties: The Leading Edge, **28**, no. 1, 28–33, doi:10.1190/1.3064143.

Korneev, V. A., G. M. Goloshubin, T. M. Daley, and D. B. Silin, 2004, Seismic low-frequency effects in monitoring fluid-saturated reservoirs: Geophysics, **69**, no. 2, 522–532, doi:10.1190/1.1707072.

Kuster, G. T. and M. N. Toksöz, 1974, Velocity and attenuation of seismic waves in two-phase media: Part II. Experimental results: Geophysics, **39**, no. 5, 607–618, doi:10.1190/1.1440451.

Lambert, M.-A., T. T. Nguyen, E. H. Saenger, and S. M. Schmalholz, 2011, Spectral analysis of ambient ground-motion – Noise reduction techniques and a methodology for mapping horizontal inhomogeneity: Journal of Applied Geophysics, **74**, no. 2-3, 100–113, doi:10.1016/j.jappgeo.2011.04.007.

Müller, T. M. and E. Rothert, 2006, Seismic attenuation due to wave-induced flow: Why Q in random structures scales differently: Geophysical Research Letters, **33**, no. 16, L16305, doi:10.1029/2006GL026789.

Narváez, A., T. Zauner, F. Raischel, R. Hilfer, and J. Harting, 2010, 2010, Quantitative analysis of numerical estimates for the permeability of porous media from lattice-Boltzmann simulations: Journal of Statistical Mechanics, P11026, doi: 10.1088/1742-5468/2010/11/P11026.

O'Connell, R. and B. Budiansky, 1974, Seismic velocities in dry and saturated cracked solids: Journal of Geophysical Research. Solid Earth, **79**, no. 35, 5412–5426, doi:10.1029/JB079i035p05412.

Pride, S. R., J. G. Berryman, and J. M. Harris, 2004, Seismic attenuation due to wave-induced flow: Journal of Geophysical Research. Solid Earth, **109**, B1, B01201, doi:10.1029/2003JB002639.

Quintal, B., S. M. Schmalholz, and Y. Y. Podladchikov, 2011a, Impact of fluid saturation on the reflection coefficient of a poroelastic layer: Geophysics, **76**, no. 2, N1-N12, doi: 10.1190/1.3553002.

Quintal, B., H. Steeb, M. Frehner, and S. M. Schmalholz, 2011b, Quasi-static finite element modeling of seismic attenuation and dispersion due to wave-induced fluid flow in poroelastic media: Journal of Geophysical Research. Solid Earth, **116**, B1, B01201, doi:10.1029/2010JB007475.

Ruiz, F. and A. Cheng, 2010, A rock physics model for tight gas sand: The Leading Edge, **29**, no. 12, 1484–1489, doi:10.1190/1.3525364.

Saenger, E. H., F. Enzmann, Y. Keehm, and H. Steeb, 2011, Digital rock physics: Effect of fluid viscosity on effective elastic properties: Journal of Applied Geophysics, **74**, no. 4, 236–241, doi:10.1016/j.jappgeo.2011.06.001.

Saenger, E. H., S. M. Schmalholz, M.-A. Lambert, T. T. Nguyen, A. Torres, S. Metzger, R. M. Habiger, T. Müller, S. Rentsch, and E. Méndez-Hernández, 2009, A passive seismic survey over a gas field: Analysis of low-frequency anomalies: Geophysics, **74**, no. 2, O29–O40, doi:10.1190/1.3078402.

Smith, T. M., C. M. Sayers, and C. H. Sondergeld, 2009, Rock properties in low-porosity/low-permeability sandstones: The Leading Edge, **28**, no. 1, 48–59, doi:10.1190/1.3064146.

Taner, M. T., F. Koehler, and R. E. Sheriff, 1979, Complex seismic trace analysis: Geophysics, **44**, no. 6, 1041–1063, doi:10.1190/1.1440994.

Tisato, N., C. Madonna, B. Artman, and E. H. Saenger, 2011, Low frequency measurements of seismic wave attenuation in Berea sandstone: 81st Annual International Meeting, SEG, Expanded Abstracts, 2277–2281, doi:10.1190/1.3627661.

White, J. E., 1975, Computed seismic speeds and attenuation in rocks with partial gas saturation: Geophysics, **40**, no. 2, 224–232, doi:10.1190/1.1440520.

Corresponding author: beatriz.quintal@erdw.ethz.ch